Cluster defects in gibbsite nanoplates grown at acidic to neutral pH

SCHOLARONE™
Manuscripts

ARTICLE

Cluster defects in gibbsite nanoplates grown at acidic to neutral pH†

Sebastian T. Mergelsberg[a]*, Mateusz Dembowski[a], Mark E. Bowden[a], Trent R. Graham[a], Micah Prange[a], Hsiu-Wen Wang[b], Xin Zhang[a], Odeta Qafoku[a], Kevin M. Rosso[a], Carolyn I. Pearce[a,c]*

Gibbsite [α-Al(OH)$_3$] is the solubility limiting phase for aluminum across a wide pH range, and it is a common mineral phase with many industrial applications. But the growth mechanism of this layered-structure material remains incompletely understood. Synthesis of gibbsite at low to circumneutral pH yields nanoplates with substantial interlayer disorder. Here we examine defects in this material in detail, and the effects of recrystallization in highly alkaline sodium hydroxide solution at 80 °C. We employed a multimodal approach, including scanning electron microscopy, magic-angle spinning nuclear magnetic resonance (MAS-NMR), Raman and infrared spectroscopies, X-ray diffraction (XRD), and X-ray total scattering pair distribution function (XPDF) analysis to characterize the aging of the nanoplates over several days. XRD and XPDF indicate that gibbsite nanoplates precipitated at circumneutral pH contain dense, truncated sheets imparting a local difference in interlayer distance. These interlayer defects appear well described by flat Al$_{13}$ aluminum hydroxide nanoclusters nearly isostructural with gibbsite sheets present under synthesis conditions and trapped as interlayer inclusions during growth. Aging at elevated temperature in alkaline solutions gradually improves crystallinity, by showing a gradual increase in H-bonding between interlayer OH groups. Between 7 to 8 vol% of the initial gibbsite nanoparticles exhibit this defect, with the majority of differences disappearing after 2-4 hours of recrystallization in alkaline solution. The results not only identify the source of disorder in gibbsite formed under acidic/neutral conditions but also point to a possible cluster-mediated growth mechanism evident through inclusion of relict oligomer with gibbsite-like topology trapped in the interlayer spaces.

Introduction

Gibbsite [α-Al(OH)$_3$] is a common mineral phase and synthetic nanoparticles have numerous industrial applications, for example as adsorbents,[1] fire-retardants,[2] and precursors to other alumina phases via the Bayer process.[3-5] Gibbsite nanoparticles are also used as model Al-hydroxide phases to: (i) study wastewater treatment;[6-8] (ii) determine Al behavior during processing of highly alkaline nuclear waste;[9-11] and (iii) establish chemical controls on soil pH and water composition.[12] In most cases, such applications require targeted synthesis of nano-sized gibbsite plates through a precipitation reaction at neutral-to-low pH.[13-15] However, the crystallinity of synthetic gibbsite strongly depends on growth conditions, and growth defects are common. Gibbsite precipitated from solution at low pH conditions forms as hexagonal nanoplates that exhibit some minor defects, dependent upon the solution conditions during nucleation and growth.[3, 8, 15, 16] When exposed to alkaline solutions, gibbsite tends to grow perpendicularly to the [001] direction yielding dominant basal planes and, in some instances, develops new faces such as (101), (112), and (011).[17-20]

The basis for these defects has remained largely unresolved. Examples of the formation and importance of various defect structures in gibbsite nanoplates is rapidly emerging in the literature. Chang et al.[21] reported formation of twinned gibbsite nanoplates with textured surfaces that have since been used for the controlled synthesis of catalyst[22] materials by surface modification. Another recent study[23] demonstrated that wetting of gibbsite particles, and other surface-driven reactions, are dependent on the presence of surface defects, particularly at step edges. Computational models used to interpret spectroscopic signatures of gamma irradiated gibbsite suggest that formation of near-surface vacancies improves hydrogen bonding at the interface between gibbsite and the solution.[24, 25]

At the acidic pH values used for gibbsite nanoplate synthesis, a possible source of defects is the adsorption and incorporation of metastable solution species, such as oligomeric Al-containing clusters. Various oligomeric Al species are well known to occur in low to neutral pH solutions near gibbsite saturation although little is currently known about their possible role as precursors to gibbsite nucleation and growth.[26-32] Due to the relatively slow kinetics of gibbsite nucleation and growth,[33] it is plausible that some of these solution species may sorb to growing facets, particularly the slowest growing basal (001) surface that tends to dominate the nanoplate morphology. Although such an adsorption process would not necessarily reflect an essential part of the growth mechanism, burial and preservation of such adsorbates could at least open a window into species present during growth.

The H-bonded layered structure of gibbsite provides a novel basis for characterizing defects. Bulk gibbsite occurs as sheets of six-coordinate Al^{3+} octahedra comprising the basal (001) plane (Figure 1).[34] The two crystallographically unique Al sites (Al$_1$ and Al$_2$) are coordinated by six hydroxide (OH) sites, separated into those engaged in intra- or inter-layer hydrogen (H)-bonding. A recent ^{1}H and ^{27}Al magic-angle spinning nuclear magnetic resonance (MAS-NMR) study concluded that the Al$_1$ site, characterized by a higher quadrupolar coupling constant, is coordinated by four intra- and two inter-layer H-bonding -OH groups, while the second Al$_2$ site is coordinated by two intra- and four inter-layer H-bonded -OH groups.[35] This unique arrangement of -OH groups has a profound effect on the Raman

a. *Pacific Northwest national Laboratory, Richland, Washington 99352, USA. Email: Sebastian.Mergelsberg@pnnl.gov, Carolyn.Pearce@pnnl.gov*
b. *Oak Ridge National Laboratory, Oak Ridge, Tennessee 37831, USA*
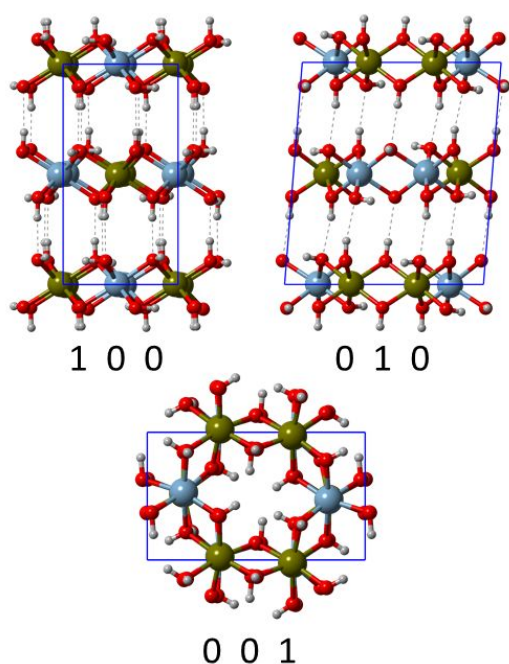c. *Washington State University, Pullman, Washington 99164*

Figure 1. Simplified crystal structure of gibbsite showing the hexagonal Al_6 unit inside of the unit cell (blue lines). Three views are shown, parallel to the three principal crystallographic axes. Note that the number of atoms shown is greater than the number of atoms in the unit cell to highlight the hexameric unit. Al_1 sites are shown in blue, Al_2 sites in dark green, oxygen in red, hydrogen in light grey, and hydrogen bonds as dotted grey lines.

and IR spectroscopic signatures of gibbsite that are commonly employed to distinguish it from its polymorph, bayerite.[36, 37]

Here we examined the defective gibbsite structure resulting from growth at pH 5, and the effects of recrystallization at the highly alkaline conditions of 3 M sodium hydroxide (NaOH) solution at 80 °C. These conditions are representative of Al-containing high-level radioactive waste (HLW) sludges,[38] currently stored in hundreds of tanks at the Department of Energy's Hanford Site (WA) and Savannah River Site (SC) and similar to those employed in the industrial Bayer process for Al oxide production.[39, 40] The structural basis for the disorder in the as-precipitated gibbsite nanoplates, and their evolution during alkaline aging, was determined using ^{27}Al MAS-NMR, Raman and IR spectroscopy, X-ray diffraction (XRD), and X-ray total scattering pair distribution function (XPDF) analysis. The findings show that the primary defect in the acid precipitated gibbsite nanoplates is related to inclusion of interlayer disk-like Al oligomeric clusters structurally similar to the repeating motif in a gibbsite sheet, which impacts the extent of order in interlayer distances between the gibbsite sheets. The results establish the defect superstructure in gibbsite nanocrystals and provide a basis for molecular scale models of gibbsite growth and reactivity.

Experimental

Materials and Methods

Synthesis of Gibbsite Nanoplates. Gibbsite nanoplates were precipitated via dissolution of an amorphous Al hydroxide precursor.[15] A solution of 0.25 M Al nitrate ($Al(NO_3)_3 \cdot 9H_2O$, ≥ 98%, Sigma-Aldrich) in water (18.2 MΩ·cm) was prepared and titrated using 1.0 M NaOH (≥ 98%, Sigma-Aldrich) until a pH of 5 was attained. The precipitated amorphous Al hydroxide precursor was stirred for 1 h at 20°C by a stir bar rotating at 120 rpm. The precipitated Al hydroxide precursor was collected by centrifugation and re-dispersed in water. This wash step was completed three times to remove adsorbed Na^+ and NO_3^- ions. After washing, the Al hydroxide precursor was dispersed in water (0.3 g pelleted gel per mL of water) and transferred to a 2 L Pyrex bottle, which was heated at 80 °C for 7 days. After 7 days, the gibbsite solids were collected by centrifugation. Because approximately 30 g of gibbsite was needed for this study, synthesis yields were improved by placing the supernatant into a new 2 L Pyrex bottle and heating the solution at 80 °C for an additional 7 days. The gibbsite precipitated in the first and second aliquots was washed by centrifugation, and re-dispersed in water three times, then dried in an oven at 80 °C overnight. The second precipitation step resulted in insignificant changes in the initial spectroscopic signatures of gibbsite (See Section S1 in the SI).

Aging of Gibbsite Nanoplates. To evaluate the effect of aging gibbsite in alkaline NaOH solution over time, twelve Teflon-lined Parr vessels were prepared by the addition of 1.87 g of gibbsite to 10 mL of 3 M NaOH. The twelve Parr vessels were then heated for 0.5, 1, 2, 3, 4, 5, 6, 24, 48, 72, 96, or 144 hrs in a rotary oven at 80°C operating at 10 rpm. After the elapsed time, the Parr vessels were removed from the oven and allowed to cool for 60 min. The gibbsite solids were vacuum filtered, washed with water, and dried at 50 °C in an oven.

[27]Al Magic Angle Spinning Nuclear Magnetic Resonance Spectroscopy. ^{27}Al MAS NMR spectroscopy was conducted on a Bruker NMR spectrometer at a field strength of 14.1 T using a 2.5 mm MAS probe. Gibbsite was loaded into the 2.5 mm rotor, which was equipped with Vespel tip and drive shafts. Spectra were acquired with 20.0 kHz spinning rate. ^{27}Al MAS NMR spectra are referenced to 1 M $Al(D_2O)_6^{3+}$, which was prepared by dissolving anhydrous Al chloride ($AlCl_3$, < 99%, Sigma Aldrich) in D_2O (99.9% Atom % D, Sigma Aldrich). The spectra were acquired following the application of a single 0.45 μs pulse, the length of which corresponds to a $\pi/20$ pulse length for the $Al(D_2O)_6^{3+}$ reference. The acquisition time was 18.6 ms, the recycle delay was 1 s, and 4,096 transients were collected. The spectra were analyzed in Mestrenova (v14.0.1) where 5 Hz of exponential line broadening was applied. Based on previously published limits of detection for >80,000 transients,[41] the limit of detection of non-crystalline Al[6] species is estimated at approximately 2 % in this study, assuming the main contaminant is the flat-Al13 cluster.[42, 43] Similarly, the detection limit for tetrahedral Al species is approximately 0.5 %.

Fourier-Transform Infrared (FTIR) Spectroscopy. FTIR spectroscopy measurements were performed in transmission mode using a Bruker Vertex 70. Each measurement consisted of 256 scans taken from 400 to 4000 cm^{-1} with a resolution of 4 cm^{-1}. Samples for measurements were prepared by mixing with KBr and pressed into a pellet prior to analysis.

Raman Spectroscopy. Raman spectra were obtained using a Horiba LabRam HR spectrometer in the 3000-3700 cm^{-1} spectral region using a 633 nm continuous light source and a 40x optical objective mounted on a Nikon Ti-E inverted microscope. Each spectrum consists of an average of ten, 60 second exposure times characterized by 4 cm^{-1} resolution.

Surface Area Analysis. Specific surface area and porosity was determined using a Quantachrome Autosorb-1 with nitrogen as the adsorbate. Prior to analysis, material was baked at 100 °C overnight on the degassing station of the instrument to remove excess surface adsorbed species. Surface area was determined using the Brunauer-Emmett-Teller (BET) methodology.

X-ray Diffraction. XRD patterns were acquired on a Philips X'pert Multi-Purpose diffractometer (PANAlytical Almelo, The Netherlands), equipped with a fixed Cu anode operating at 40 mA and 50 kV. Refinements were conducted in TOPAS (v5, Bruker AXS) using the published gibbsite structure,[34] line shapes calculated by the fundamental parameters approach,[44] and intensities corrected for preferred orientation of the plate-like particles. Anisotropic line broadening for crystallite size was applied using the TOPAS macros published by Ectors *et al.*,[45] and for strain using the Stephens model[46] available in TOPAS. After some experimentation the "trigonal, high 2" setting was found to provide a suitable balance of good fitting with few refineable parameters.

Following initial application of the Stephens model an explicit layer-stacking model was used to gain insight into the origin of the strain. These models contained occasional interlayer spacings either shorter or longer than normal (obtained from the 144 hour aged sample) in an otherwise perfect gibbsite lattice. The gibbsite ···ABAB··· stacking was maintained in all models. The procedure, available in TOPAS, generated 100 pseudorandom supercells, each of 300 gibbsite layers containing defect interlayer spacings defined by a preset probability. Although these probabilities could not be refined, the defective interlayer spacings were refined along with the cell parameters, crystallite dimensions, and preferred orientation. Magnitudes of the defect spacings were not constrained in the least-squares refinements, and therefore minima where either the "short" or "long" spacings were the same as the bulk gibbsite would become apparent. The defect probability was estimated from a sequence of refinements with differing probabilities to find the best overall fit with experimental data.

The R_{wp} fit index, which weights the differences between observed ($Y_{obs,i}$) and calculated ($Y_{calc,i}$) intensities, was determined over the entire pattern using the following equation:

$$R_{wp} = \sqrt{\frac{\sum_i w_i (Y_{obs,i} - Y_{calc,i})^2}{\sum_i w_i Y_{obs,i}^2}} \qquad (1)$$

The weighting factors w_i are the square roots of the measured counts at each of the i data points. Contour plots of R_{wp} for various probabilities of the short and long interlayer spacings are shown in Fig. S10 for aging times of 0, 0.5 and 1 hour.

Total X-ray scattering for Pair Distribution Function analysis. Total X-ray scattering for PDF analysis (XPDF) was completed at the Advanced Photon Source (APS), beamline 11-ID-B.[47] Sample powders were loaded into 2 mm ID polyimide capillaries and both the sample-to-detector distance as well as the detector non-orthogonality were calibrated using a ceria (CeO$_2$) standard (NIST diffraction standard set 674a) diluted 1:25 with glassy carbon. The scattered radiation (energy of ~58.6 keV, λ = 0.2114 Å) was measured in transmission mode using an amorphous silicon (Si) detector system manufactured by Perkin Elmer TM (2048×2048 pixels, 200×200 µm^2 pixel size).

The program GSAS-II was used to sum 2D scans and perform integration to one dimensional (1D) profiles using a polarization correction.[48] PDF profiles were calculated in PDFgetX3,[49] assuming limited sodium (Na) solubility in gibbsite.[17] The CeO$_2$ standard was used to refine instrument parameters for the relevant q range (0.55 to 26 Å^{-1}) in PDFgui.[50] PDF of model structures was calculated using the DISCUS program with refined instrument parameters.[51] Linear combination fitting was done in R, optimizing the solution for the smallest chi square, allowing all possible combinations of component spectra. Differential PDF profiles (D(r)) were calculated by subtraction of the 144 hr sample pair distribution function (G(r)$_{144hr}$), from the pair distribution function of the sample of interest (G(r)$_i$):

$$D(r) = G(r)_i - G(r)_{144hr} \qquad (2)$$

Scanning Electron Microscopy. A Helios NanoLab 600i scanning electron microscopy (SEM, FEI, Hillsoboro, OR) was used to examine the gibbsite nanoplates before and after ageing in alkaline solution. The samples were sputter coated with approximately 5 - 10 nm of carbon before imaging.

Results and Discussion

Physical characteristics of initial gibbsite and after recrystallization in alkaline solution.

SEM images show that the as-synthesized gibbsite nanoplates were ~10 to 30 nm thin, highly aggregated particles, tens to hundreds of nanometers wide (Figure 2A). Upon aging in 3 M NaOH at 80 °C, the thin gibbsite nanoplates grew into distinct, thicker plates after longer reaction times (Figure S2). At t =144 hrs the plates had grown to a thickness of approximately 100 nm (Figure 2B), although widths parallel to the (001) basal surface of the particles appear similar for all time points. However, instances of some much
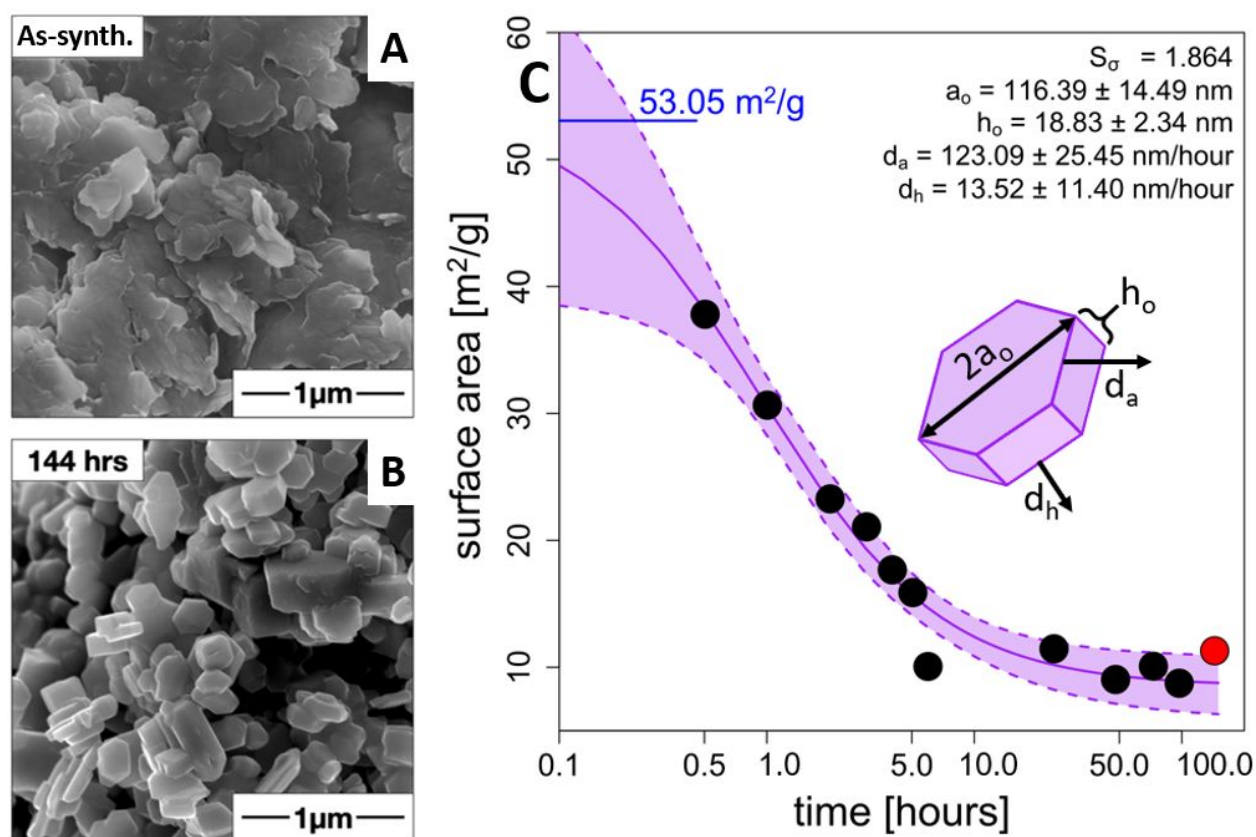
Figure 2. SEM images of A) as-synthesized gibbsite and B) after 144 hrs of reaction with 3M NaOH at 80 °C. Each sample was filtered, washed with water, and dried prior to imaging. C) Surface area vs. reaction time. The purple line represents fit of second surface area model to the data using equation S10 (SI), assuming hexagonal plates growing both parallel and perpendicular to the basal (001) surface. The standard error of the fit is S = 1.864 and the shaded area represents the 2σ error of the mean (95% confidence interval). The fitting approach is detailed in section S2 of the SI. The surface area of the as-synthesized material is shown in blue, the 144 hr sample in red.

larger particles (> 1μm) are also noted. BET analysis show the initial precipitates have an average surface area of 53.05 ± 0.54 m^2/g. This measurement is approximately in agreement with previous studies, which report surface areas of 42.4 to 47.4 m^2/g for gibbsite produced at 80-85 °C using similar methods.[3, 8, 16]

To determine the initial size and quantify relative growth rates of gibbsite nanoplates, the BET data were fit using two geometric growth models (Figure 2C, section S2), which are based on the assumption that gibbsite nanoplates can be described as free (not overlapping) regular hexagonal prisms. In the first model, growth was constrained to only occur perpendicular to the basal surface. This model predicted the formation of columnar particle shapes after 4 hours, but these shapes were not observed by SEM (Figure S3). Thus, a second model was fit to the data that accounts for growth in both particle width (parallel to (001)) and thickness (perpendicular to (001)). From the fit parameters, initial average particle sizes are estimated to be 232.8 ± 29.0 nm parallel to (001) and 18.83 ± 2.34 nm perpendicular to (001). These estimates are in good agreement with a previous study using a similar synthesis method, which reports nanoplate widths of 280 ± 35.0 nm and thickness values between 10 and 20 nm.[15] The model predicts an initial particle growth during the first hour of reaction of

246.2 ± 50.9 nm/hour parallel to (001) and 13.52 ± 11.40 nm/hour perpendicular to (001).

Studies of gibbsite growth under supersaturated conditions show higher overall growth rates, but similar differences in growth rates between the direction parallel to (001) and the direction perpendicular to (001) of approximately one order of magnitude.[33, 52] The relatively slow predicted rates and changing aspect ratio (Figure S3B) suggest gibbsite growth under these conditions occurs by classic monomer-by-monomer crystal growth kinetics. Unlike particle-mediated growth, classical growth is unlikely to introduce new long-range structural defects into the growing gibbsite nanoplates, but may propagate some existing defects, such as twinning, dislocations, and growth hillocks.[53]

Evolution of Al site symmetry by 27Al MAS NMR

^{27}Al MAS-NMR was used to resolve Al speciation in as-synthesized gibbsite and after ageing for various durations in 3 M NaOH at 80 °C. Specifically, interactions between the nuclear quadrupole moment arising from [27]Al spin of 5/2 with local electric field gradients (EFG) lead to characteristic signal broadening. Furthermore, the chemical shift of [27]Al is coordination sensitive with i) *six-coordinate* Al showing isotropic shifts from -21 to + 37 ppm, ii) *five-coordinate* Al from
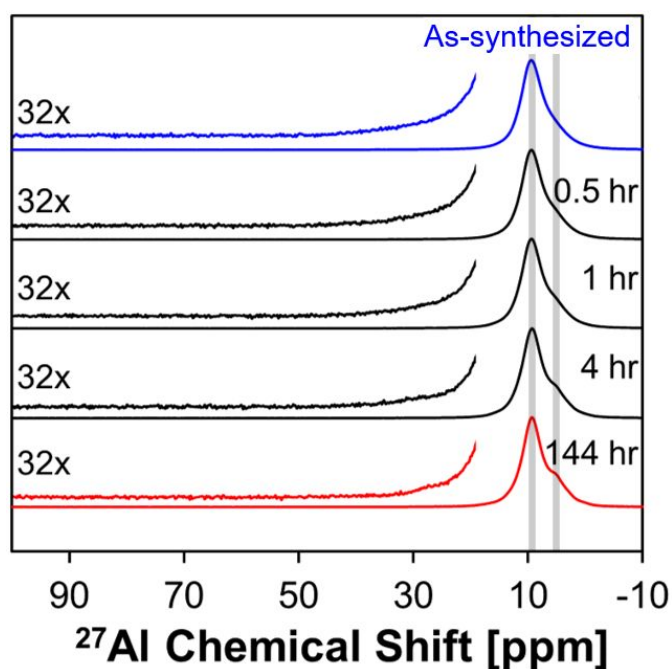
Figure 3. Comparison of ^{27}Al MAS-NMR spectra for as synthesized gibbsite (blue), and for gibbsite after reaction in 3M NaOH at 80 °C (red). Vertically scaled spectra are overlaid with 32x magnification to highlight the lack of significant quantities of tetrahedral-coordinated Al. The grey lines indicate the location of the peaks centered at ca. 9 ppm and ca. 5 ppm in the 144 hr sample.

+20 to +52 ppm, and iii) *four-coordinate* Al from +39 to + 80 ppm.[54, 55] Since the ^{27}Al MAS-NMR spectra of amorphous aluminum hydroxides contains four and five-coordinate Al sites,[42] the technique can be used in combination with X-ray scattering/diffraction to

evaluate the crystallinity of as-precipitated and aged gibbsite nanoplates, as well as, amorphous phases.

A comparison of as synthesized and aged (up to 144 hrs at 80°C in 3 M NaOH) gibbsite nanoplates is shown in Figure 3. All spectra show a broad asymmetric signal centered at ca. 9 ppm, consistent with the presence of six-coordinate Al in gibbsite.[42] There is also a clear change in peak width as a function of reaction time, highlighted by the emergence of a shoulder at ca. 5 ppm in the aged (144 hrs) gibbsite. Subtle changes in peak width and peak shape correspond to changes in the quadrupole coupling constant (C_Q) and asymmetry parameter (η). Other factors, such as the presence of other six-coordinate Al species present either on the surface or encapsulated within gibbsite sheets would give rise to signals in the octahedral Al region near 10 ppm. However, resolving the contribution of trace species from small differences in the gibbsite [27]Al resonances – due to C_Q and η – was not attempted. Given the number of variables and the magnitude of differences between samples, no meaningful fit to the data could be achieved.

Given the distribution of species as a function of pH in hydrolysis of Al^{3+}, four-coordinate Al would not be expected in the as-precipitated sample at pH ~ 5. [15] At slightly acidic pH, the Al in solution is primarily six-coordinate with a small fraction of five-coordinate species.[56] In the 3 M NaOH solutions used for

ageing, the four-coordinate aluminate complex $Al(OH)_4^-$ dominates.[17, 18] There were, however, no observable signals corresponding to five- or four-coordinate Al occurring around 20 and 80 ppm in the as-precipitated or aged gibbsite, demonstrating the lack of significant quantities of those Al coordination environments in the gibbsite sample series. The presence of other six-coordinate Al species in the form of adsorbed $Al(H_2O)_6^{3+}$ or co-crystallized gibbsite polymorphs= cannot be exclusively ruled out from only the ^{27}Al MAS-NMR data. The presence of crystalline Al oxyhydroxide species, such as bayerite or boehmite, was evaluated using X-ray scattering techniques (see later sections), which are expected to show greater sensitivity to these phases.[57-59]

OH group disorder resolved by vibrational spectroscopies

Raman and IR spectroscopy were used to provide information on the difference between the intra- and inter-layer order in the as-precipitated and aged gibbsite nanoplates (Figure 4A, B). Specifically, Raman spectra of the as-synthesized gibbsite nanoplates (t = 0 hrs) reveal four unique signals located at ca. 3365 and 3436 cm^{-1} corresponding to OH-bonds involved in inter-layer H-bonding (located perpendicular to the (001) plane), and 3527 and 3620 cm^{-1} corresponding to OH-bonds involved in the intra-layer H-bonding (located within the (001) plane). The signals observed at ca. 3365 and 3527 cm^{-1} are each comprised of two bands as evidenced by their asymmetry, which becomes easier to discern in samples aged for longer times (Figure 4A). The total of six –OH bands observed in Raman spectra is in agreement with prior ab initio and independent spectroscopic studies.[36, 60] A lack of additional bands in the low-wavenumber region (Figure S4),[37] and at ca. 3450, 3550, and 3652 cm^{-1}, rules out the presence of boehmite and bayerite, respectively, in the samples.[37] Following aging in 3 M NaOH, the –OH signatures of gibbsite become significantly sharper at 3365 and 3436 cm^{-1}, corresponding to OH-bonds perpendicular to the $Al(OH)_3$, when compared to those located at 3527, and 3620 cm^{-1}, which correspond to in-plane OH-bonds.

The relative populations of OH-groups were estimated by integrating and comparing the areas under the respective peaks (Figure 4C). In the as-precipitated gibbsite nanoplates, the majority of OH groups are located within the plane, whereas after 144 hrs of ageing there is, on average, a transition to the majority of OH groups located perpendicular to the plane. The largest difference occurs between the as-synthesized material and the sample after 6 hrs of ageing, where the population distribution changed from a minority of OH groups to ca. 52 % of OH groups located perpendicular to the plane. Note that numbers calculated by this analysis overestimate the 50% of OH-groups oriented perpendicular to the (001) plane predicted by the bulk structure of gibbsite.[34] This is likely due to variations in surface area, hydration of near-surface layers, and aspect ratio, given the large decrease in surface area during sample aging (Figure 2C).

The inversion point for signals located at 3620 and 3436 cm^{-1} (Figure S5A) occurs after ca. 24 hrs of aging while that for the combined signals at 3519/3527 and 3365/3370 cm^{-1} (Figure
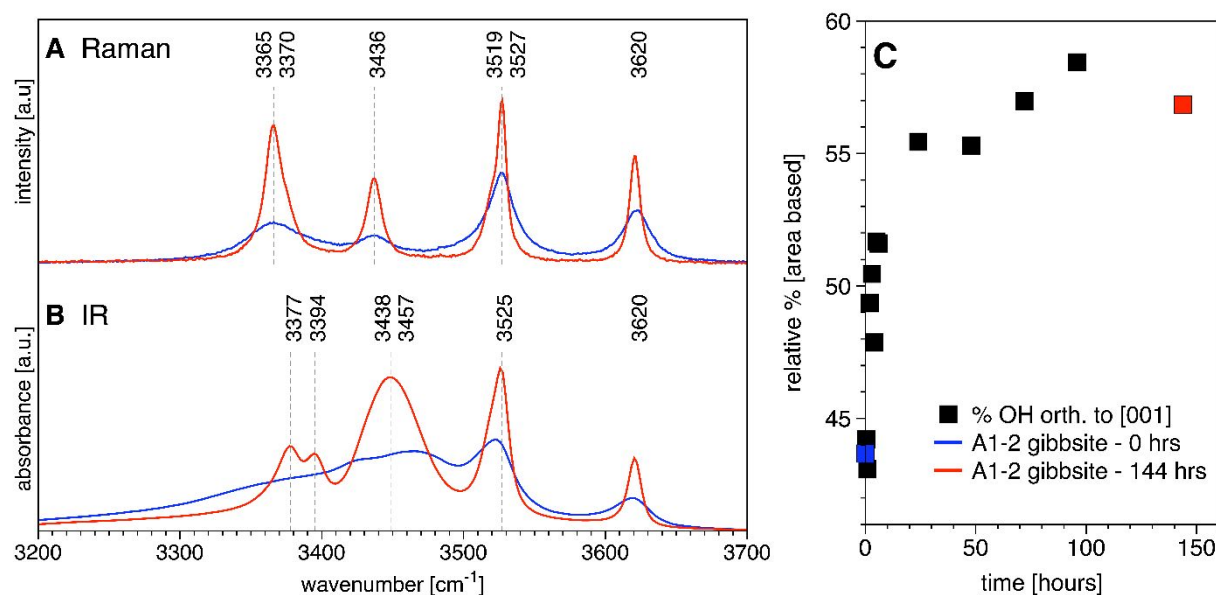
ARTICLE

Figure 4. A) Comparison of Raman spectra of as-synthesized gibbsite (blue) and after 144 hrs in 3M NaOH (red). B) FTIR spectra of unreacted gibbsite (blue) and of the same solid after 144 hours of reaction (red). C) Percent population of all hydroxide groups (based on integrated area ratio) that orient perpendicular to the (001) plane of gibbsite, as a function of reaction time. After just a few hours, ~57% of OH groups are perpendicular to the (001) plane, a stable configuration up to 144 hours.

S5B) occurs at ca. 2 hrs. Similar deconvolutions of IR spectra, including comparison of peak positions, peak widths, and integrated peak areas did not yield reasonable results due to considerable peak overlap and variable water content evident from a shoulder at ca. 3300 cm^{-1} (Figure 4B). Qualitatively, however, IR spectra did show a progressive decrease in peak full width at half maximum (FWHM) as a function of ageing time, consistent with an increase in overall crystallinity. Results from optical spectroscopy thus suggest a major source of initial disorder in gibbsite nanoplates is captured by the directionality of −OH groups. Approximately 2 to 24 hours of ageing time are necessary for the groups to reach the thermodynamically preferred orientation.

Evolution in defect density by XRD

XRD patterns of samples aged for different times were collected and refined to identify and quantify the disorder in gibbsite nanoplates. Results show increasing crystallinity during the aging of the gibbsite in solution (Figure S6). After extensive aging, the peaks were relatively sharp and good Rietveld fits could be obtained using only isotropic size broadening (~74 nm crystallites) to account for the observed peak shapes (Figure S7A). The as-precipitated nanoplates, and those aged for shorter times, had considerably broader diffraction peaks that were not fit well using an isotropic size/strain model (Figure S8), suggesting an anisotropic effect. For example, the (002) peak was broadened considerably relative to the (110) or (200), even though these peaks are all in a narrow 2θ range (Figure S9).

This broadening could not be explained solely by anisotropic crystallite dimensions, as can be seen by the substantial difference remaining in Rietveld fits (Figure S7B). Much better fits to the XRD patterns were obtained by adding anisotropic microstrain broadening (Figure S7C), and these were used to

determine the cell parameters as a function of aging time (Figure 5). Distinguishing microstrain broadening from finite size broadening becomes more reliable with data collected over a larger 2θ range, and the substantial improvement we observed with our systematic approach illustrated by Figure S6 gave us confidence in the results. The largest difference in unit

cell parameters occurs in the first 4 hours with a smooth variation which corresponds well to the kinetics of OH-group distributions observed with Raman spectroscopy (Figure 4C). Although the anisotropic strain model provided excellent Rietveld fits to the XRD data, it is difficult to use this approach to derive a mechanistic or structural understanding. Guided by the observation that the greatest microstrain broadening occurred along the *c* direction, and the results from Raman spectroscopy, variations in inter-layer spacing that could account for the observed trend in refinement parameters were investigated. This experimental approach is summarized in the

spacings) are correlated, and it seems reasonable that a single defect might introduce a locally short stacking immediately below the defect and a long stacking immediately above. This also suggests there is a single defect rather than two different defects with similar probabilities. The refinement model was therefore modified to generate defects with a single probability giving rise to sequential shorter and longer interlayer spacings. The fit index as a function of this probability is plotted in Figure 6A for samples aged up to 4 hours.

The defect probability decreased with increasing aging, and approached zero after approximately 4 hours, consistent with
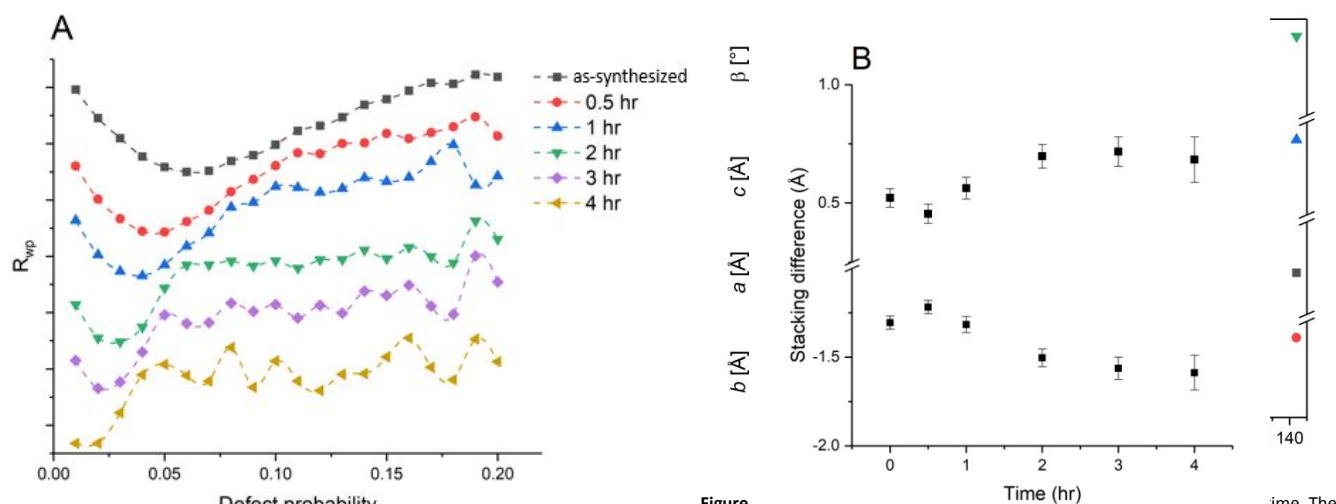

Figure 6. A) Fit index, R_{wp}, as a function of defect probability shows an increased probability of defect sites for sharp-plate gibbsite. The probability appears to have reached values (B) The refined stacking difference of the defect model as a function of aging time suggests the defect concentration rapidly increased during the first 30 min, followed by a gradual defect annealing.

Experimental Methods section and essentially involves introducing occasional shorter or longer interlayer distances between adjacent gibbsite sheets. Such defects will broaden the (001) peaks but have little effect of the breadth of (hk0) peaks, in line with our observations.

First, both shorter or longer defects were introduced with independent probabilities and spacings. Although the lattice parameters (Figure 5) showed that the average c dimension was smaller for short aging times, it was anticipated that defects with only shorter layer spacings would be difficult to explain by any structural model. Further, the model refined the difference in layer spacing for both the shorter and longer defects, and if longer defects were not useful for predicting the observed diffraction pattern, the refined spacing would approach the non-defect value. The agreement with experimental patterns, quantified by the fit index R_{wp}, is shown in Figure S10 for different defect probabilities in the first 3 aged samples. Two trends are immediately apparent for the best fits (Figure S10A, lowest R_{wp}). Firstly, the probabilities of short and long spacings are approximately equal and secondly, this probability becomes smaller with increasing aging time. The second trend is intuitive from the observation noted above that the XRD pattern approaches unstrained gibbsite with increasing aging time, and that the majority of this change occurs with the first 4 hours. The first trend suggests that the two defects (short and long

how well the XRD patterns matched ideal gibbsite. The magnitude of the layer displacements showed a small increase with aging time; however, these parameters are likely correlated with other refined quantities and the change was not considered significant. The locally short spacing had a larger change (ca. -1.5 Å) than the locally larger spacing (ca. +0.7 Å), Figure 6B.

It must be stressed that this modelling of the diffraction data with layer spacing defects is designed to capture the large-scale behavior of gibbsite over a sample average, and not to be an atomically accurate model. Differences in the spacing between layers implies a different interlayer atomic arrangement or structural changes within the layer which cannot be robustly refined in a Rietveld model. This XRD-derived model, however, provides valuable clues for potential atomic-level causes for the anisotropic microstrain, which affects the diffraction patterns through defects in layer stacking. These defects are best probed through spectroscopic (previous section) and total scattering experiments (following section).

Development of atomic scale models of disordered gibbsite from PDF analyses.

X-ray total scattering patterns reflect an increase in gibbsite crystallinity with reaction time, consistent with the XRD findings (Figure S11A). Calculation of the PDF profile from the scattering

data further determines differences between the samples (Figure S11B) on an atomic scale. For example, comparison of the short-range order (r < 4 Å) of the samples highlights that the degree of disorder is relatively small, i.e. the aged sample is a relatively good fit to the as-synthesized sample (Figure 7A). The Al–O (1.9 Å), O–O (2.79 Å), Al–Al (2.91 Å), and secondary Al–O (3.58 Å) distances approximately line up between samples, with the exception of a small shift in the composite O–O and Al–Al peak from 2.84 Å in the as-synthesized material to 2.86 Å after 144 hrs of reaction time (Figure 7A).
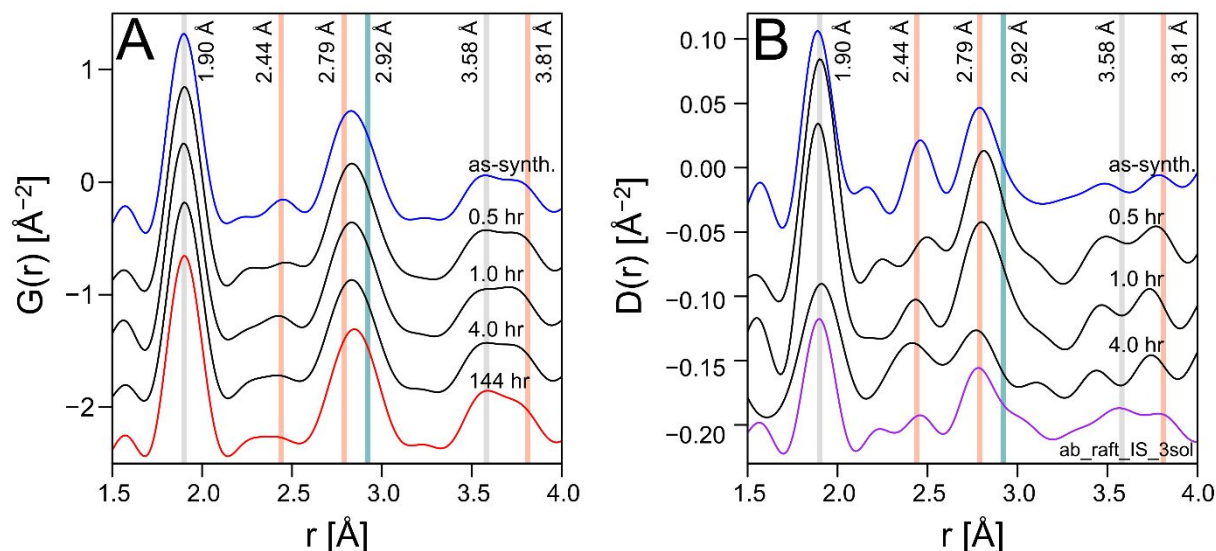

Figure 7. A) Pair Distribution Function (PDF) of the as synthesized gibbsite (blue) and of the gibbsite sample at t = 0.5, 1, and 4 hr (black), and t = 144 hr (red), highlighting the region from 1.5 to 4 Å. G(r) profiles are offset by 0.5 Å^{-2}. B) Scaled differential PDF profiles of the as synthesized sample (blue) and of the samples at t = 0.5, 1, and 4 hr (black) were obtained by subtracting the 144 hr sample total scattering signal from the respective samples and calculating the PDF from the differential diffraction pattern. The calculated model structure ab_raft_IS_3sol (purple) has the lowest reduced χ^2 value when compared to the differential PDF profile at t = 0.5 hr. Lines represent the position of dominant peaks and represent the Al–O (grey; 1.9 Å, 3.58 Å), O–O (orange; 2.44 Å , 2.79 Å, 3.81 Å), and Al–Al (teal; 2.92 Å) distances. D(r) profiles are offset by 0.05 Å^{-2}.

To resolve these small differences between the samples, differential PDF profiles were calculated from the difference in scattering intensity of each sample compared to the sample at t=144 hr (Figure 7B). Results reveal significant differences in the intensities and average value of the Al–O, O–O, Al–Al, and secondary Al–O distances. For example, all samples aged for one hour or less show a residual primary Al–O distance that decreases in intensity at t = 4 hr. This indicates that early in the reaction, gibbsite nanoplates contain additional Al sites, compared to the sample t = 144 hr. In addition, the differential PDF (D(r)) demonstrates additional O–O distances are present in the samples, without a similar Al-Al signal. Given that ^{27}Al NMR indicates that all Al is octahedrally coordinated in these samples, the additional Al sites are constrained to 6-coordinate Al and are likely to include vacant lattice sites, truncated sheets, and a disruption in inter-layer distances. These small features would increase O–O and Al–O distances without a similar increase in Al–Al. Based on these and similar insights from the medium- to long-range differences between samples, a large matrix of potential defect structures was developed (Table S2). Structural defect models are based on common stacking faults, adsorbed oligomeric alumina species, and filled interstitial sites, and are not energy-minimized. Calculated profiles of short-range defects, such as very small single-layer sheets, show the greatest similarity to the measured D(r) signal (e.g. configuration ab_raft_IS_3sol; purple in Figure 7B).

Table 1. Results of the LCF model to gibbsite nanoplates up to r = 16 Å, as a function of reaction time. The gibbsite reference structure used in the fit is the sample after 144 hrs of reaction. Only one defect model structure, ab_raft_IS_3sol, is needed to explain the remaining 4-9 vol%, with a variable stacking difference. V_{exp} is the vol% of the defect expected from the geometric growth model (Figure 2C), assuming no annealing occurs after 0.5 hours.

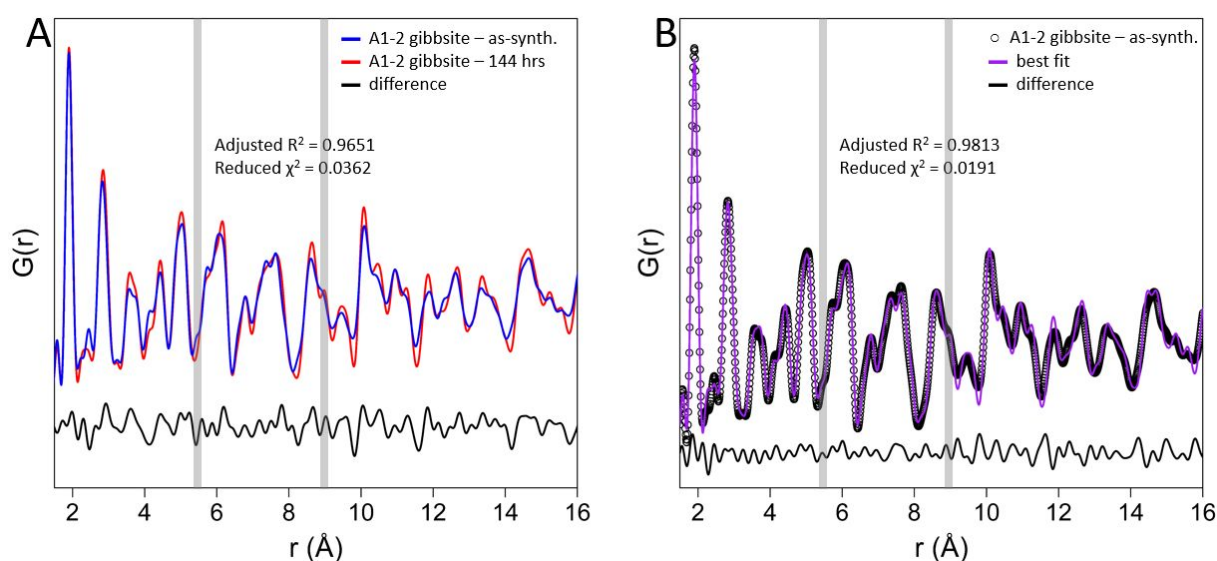| Reaction time (hr)	144 hr Gibbsite (vol%)	ab_raft_IS_3sol (vol%)	Stacking diff. (Å)	V_{exp} (vol%)	Adj. R^2	Red. χ^2
0	92.3	7.7	− 0.2	–	0.9813	0.01912
0.5	91.3	8.7	− 0.3	8.7	0.9892	0.01099
1	96.2	3.8	− 0.3	3.9	0.9887	0.01205
2	100	0	--	1.3	0.9929	0.00743
3	100	0	--	0.6	0.9904	0.00999
4	100	0	--	0.4	0.9936	0.00786

Figure 8. A) Pair Distribution Function (PDF) of the initial (blue) and final (red) gibbsite samples. The difference between profiles is shown in black, along with R2 and χ2 that describe the similarity between the signals. B) Linear combination fit (LCF) of model structures (purple) to the PDF profile of the as synthesized sample (black circles). The differential pattern is shown as a black line. See Table 1 for further details. Grey bands highlight shoulders at 5.5 and 9 Å.

ARTICLE

Using the complete set of calculated PDF profiles, we fit the experimental G(r) by linear combination fitting (LCF). The differences between profiles are approximately independent of r and the magnitude of differences between samples at t=144 hrs and the as synthesized sample is relatively small (Figure 8A). Results of the LCF are summarized in Table 1. The fit (Figure 8B) accounts for the majority of differences between samples and captures small features, for example the shoulders at 5.5 Å and 9 Å (Figure 8B, grey bars), that are absent in the annealed sample. Specifically, the refined model predicts the as-synthesized sample is composed of 92.3 vol% annealed gibbsite and 7.7 vol% of the signal is attributed to a single defect structure, ab_raft_IS_3sol_2. This configuration is a hexameric ring of alumina octahedra with the central interstitial site ("C-site") filled and 3 additional alumina octahedra above the structure, shifted 0.2 Å closer to one layer relative to regular stacking (Figure 9). The model without any out-of-plane Al-O octahedra (grey atoms in Figure 9) does not affect the fit. This particular structure was modified from the previously published flat Al_{13} structure (Figure S12).[28, 30-32] Using a smaller fit window

reaction, the samples are well-fit by a 0 to 3% defect probability. With both the PDF LCF model and the XRD model, the defect magnitude (stacking difference) increases from the as synthesized sample to the sample after 0.5 hr reaction; this is likely due to the "surface-inward" mechanism for gibbsite crystallization,[42] with the outermost crystalline region preferentially dissolved during the initial 0.5 h. The major difference between models is the magnitude of the mis-stacking, which is likely due to differences in sample analysis volume, as XRD is weighted towards defects in otherwise ordered domains, whereas PDF analysis includes signal from near-surface and more disordered domains. Careful examination of the PDF fit reveals the peak heights of long-range features are overestimated by the LCF model (Figure 8B), which may correlate with the smaller surface area to volume ratio of the aged samples compared to the as-synthesized gibbsite (Figure 2C). The larger the surface contribution to the PDF profile, the less sharp the peaks will be due to increased motion of the atoms in a given interatomic distance. Thus, the LCF analysis is weighted towards the short- to medium-range
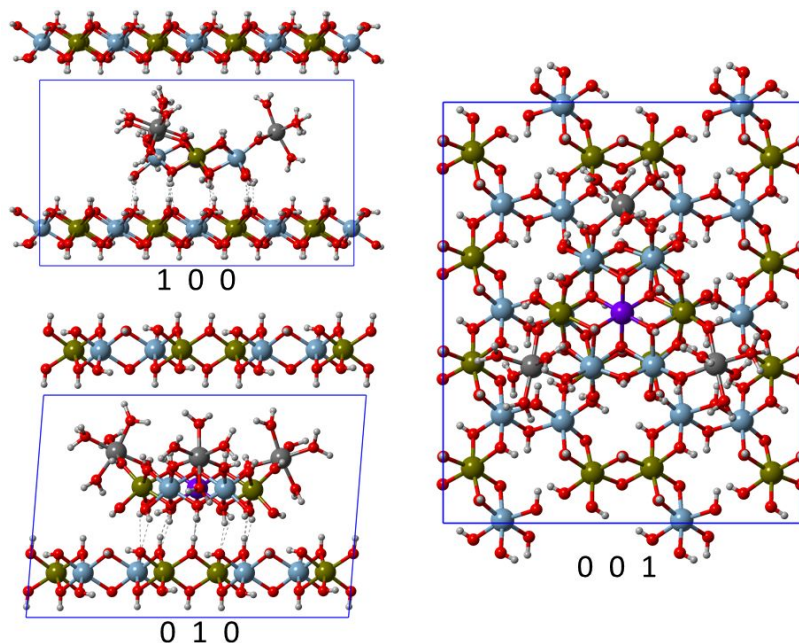

Figure 9. Example of one of the model structures, ab_raft_IS_3sol, viewed in a 2 x 2 x 1 supercell (blue) along the a (100), b (010), and c (001) axes. Al_1 sites are labeled in light blue, Al_2 in dark green, Al_3 (or "C sites") in purple, and hydrated Al atoms in grey. Oxygen atoms are red and hydrogen atoms are light grey.

indicates that a simple model of reduced inter-layer distances, similar to the XRD model, is able to account for a lot of the disorder (Table S3). However, error estimates are significantly better at medium- to long-range order for configurations with sheets that are shortened in the a and/or b direction ("truncated"), eventually converging on ab_raft_IS_3sol. Note that no models based on stacking sequence errors (i.e. ···ABBA··· stacking instead of ···ABAB···) affect the fits.

Comparison of the PDF LCF model to the XRD model shows relatively good agreement in several aspects: (i) the defect probability of the as synthesized sample is estimated at the local minimum between 6 to 7 % in Figure 6A, compared to a value of 7.7 vol% in Table 1; (ii) samples with up to one hour reaction time have defect probabilities > 3%; and (iii) after 2 hours of

order (1.5 to 10 Å) and may slightly overestimate the overall contribution of the defect. The maximum value of the defect density at a given r can be estimated by the ratio of D(r)/G(r) (Table S4). For the as-synthesized sample, the estimated maximum defect density of 7.7 vol% matches the LCF model exactly.

The collective analyses reveal that the initial gibbsite nanoplates contain misaligned, truncated sheets, consistent with relatively rapid crystallization from an amorphous aluminum hydroxide gel precursor that kinetically traps smaller clusters between layers. The best-fitting defect model, ab_raft_IS_3sol model, is based on the Al_{13} cluster, which is not stable in the highly alkaline conditions of the experiment.[29, 32, 61] Thus, the defect is most likely linked to structures deeper

within the gibbsite nanoplates. This is largely consistent with an estimate of the volume occupied by the defect (V_{max}, Table 1) if no annealing or dissolution occurs after 0.5 hours. This suggests gibbsite growth of the nanoplates in 3M NaOH at 80 °C is fast enough to reduce the defect signal below the detection limit of XRD and PDF within 2 to 3 hours. This assumes subsequent growth in alkaline conditions does not produce any further defects, suggesting growth under alkaline conditions occurs primarily by classical crystal growth processes that trap defects or surface-associated structures within the particles.

With respect to the configuration of the flat Al_{13} defect cluster, the hexameric ring of alumina octahedra is 'gibbsite-like' but, for the cluster to be incorporated into gibbsite, the Al octahedron occupying the C-site must be removed. The fact that this cluster remains trapped within the gibbsite nanoplates suggests that removal of the interstitial C-site may be the rate-limiting step in the assembly of clusters from the amorphous Al hydroxide precursor to form gibbsite at acidic to neutral pH.

Conclusions

This study highlights the nature of defect content in gibbsite precipitated at acidic to circumneutral conditions, and how the structure recrystallizes to become more ordered in 3M NaOH at 80 °C within a few hours. ^{27}Al MAS NMR spectroscopy showed that the Al remains six-coordinate throughout the entire reaction, with a decrease in line broadening as a function of time possibly i) due to an elimination of a trace poorly resolved octahedral Al species severely overlapping with the gibbsite signal, ii) a narrowing of the distribution of quadrupolar coupling parameters of gibbsite, or iii) changes in the discrete quadrupolar coupling parameters of gibbsite.

Disorder associated with OH groups that are orthogonal to the (001) lattice planes suggests initial nanoplates contain defects such as truncated sheets and disrupted inter-layer gaps that produce O–H distances unfavorable for interlayer H-bonding. This was confirmed using a rigorous fit to the XRD data. However, residual errors remained relatively high, indicating additional sources of disorder. Linear combination fitting of the PDF data established this additional disorder is likely due to dense structures with short-range coherence trapped within the gibbsite particles. These flat Al_{13}-like structures are known to be present in lower pH conditions that produce the initial gibbsite nanoplates. Thus, we propose the presence of trapped oligomeric alumina clusters in the as-precipitated gibbsite nanoplates that cause the formation of additional medium-range order defects as the sample is heated under alkaline conditions. The signals associated with the defect structures decrease within 2 to 4 hours in 3M NaOH at 80 °C, consistent with particle growth rates (Table 1). This suggests the defect structures do not heal over time, but are likely buried within the growing particles.

The finding of flat Al_{13} oligomeric interlayer inclusions in the gibbsite precipitated at acidic to circumneutral pH has important implications understanding differences in gibbsite reactivity that could result from different growth conditions. More broadly however the finding may provide clues for understanding the growth mechanism of gibbsite under acidic conditions where Al cluster formation is typical. In particular, our study raises three fundamental questions: i) do these trapped clusters represent distinct intermediates during transformation from gel to gibbsite; (ii) if the clusters are kinetically trapped, do the large array of synthesis conditions in the literature produce different defect concentrations; (iii) can these more flexible defect structures sorb and subsequently entrain other elements in the growing gibbsite particles?

Author Contributions

MD, TRG, and CIP designed the study. MD and TRG synthesized the material. TRG, MD, OQ, MEB, and STM collected and analysed the data. STM wrote the original draft of the manuscript. MD, TRG, and MEB contributed technical expertise. CIP and STM wrote the paper. STM, MD, MEB, TRG, MP, HW, XZ, OQ, KMR, and CIP reviewed and edited the manuscript.

Conflicts of interest

There are no conflicts to declare.

Acknowledgements

Notes and references

1. S. Goldberg, *Soil Science*, 2010, **175**, 105-110.
2. Y.-Y. Yen, H.-T. Wang and W.-J. Guo, *J. Appl. Polym. Sci.*, 2013, **130**, 2042-2048.
3. X. Zhang, P. L. Huestis, C. I. Pearce, J. Z. Hu, K. Page, L. M. Anovitz, A. B. Aleksandrov, M. P. Prange, S. Kerisit, M. E. Bowden, W. Cui, Z. Wang, N. R. Jaegers, T. R. Graham, M. Dembowski, H.-W. Wang, J. Liu, A. T. N'Diaye, M. Bleuel, D. F. R. Mildner, T. M. Orlando, G. A. Kimmel, J. A. La Verne, S.

B. Clark and K. M. Rosso, *ACS Appl. Nano Mater*, 2018, **1**, 7115-7128.

4. S. Liu, C. Chen, Q. Liu, Y. Zhuo, D. Yuan, Z. Dai and J. Bao, *RSC Advances*, 2015, **5**, 71728-71734.

5. P. Souza Santos, H. Souza Santos and S. P. Toledo, *Materials Research*, 2000, **3**, 104-114.

6. X. Liu, Y. Wang, X. Cui, S. Zhu and J. Cao, *Journal of Chemical & Engineering Data*, 2020, DOI: 10.1021/acs.jced.0c00815.

7. S. Sadri, B. B. Johnson, M. Ruyter-Hooley and M. J. Angove, *Applied Clay Science*, 2018, **165**, 64-70.

8. S. Louaer, Y. Wang and L. Guo, *ACS Appl Mater Interfaces*, 2013, **5**, 9648-9655.

9. J. G. Reynolds, M. Dembowski, T. R. Graham and C. Pearce, *Fluid Phase Equilibria*, 2021, **532**.

10. D. L. Herting, J. G. Reynolds and W. B. Barton, *Industrial & Engineering Chemistry Research*, 2014, **53**, 13833-13842.

11. P. Huestis, C. I. Pearce, X. Zhang, A. T. N'Diaye, K. M. Rosso and J. A. LaVerne, *J. Nucl. Mater.*, 2018, **501**, 224-233.

12. E. W. Slessarev, Y. Lin, N. L. Bingham, J. E. Johnson, Y. Dai, J. P. Schimel and O. A. Chadwick, *Nature*, 2016, **540**, 567-569.

13. H. Tang, F. Xiao and D. Wang, *Adv Colloid Interface Sci*, 2015, **226**, 78-85.

14. X. Zhang, W. Cui, K. L. Page, C. I. Pearce, M. E. Bowden, T. R. Graham, Z. Shen, P. Li, Z. Wang, S. Kerisit, A. T. N'Diaye, S. B. Clark and K. M. Rosso, *Cryst Growth Des*, 2018, **18**, 3596-3606.

15. X. Zhang, X. Zhang, T. R. Graham, C. I. Pearce, B. L. Mehdi, A. T. N'Diaye, S. Kerisit, N. D. Browning, S. B. Clark and K. M. Rosso, *Cryst Growth Des*, 2017, **17**, 6801-6808.

16. M. Sassi, Z. Wang, E. D. Walter, X. Zhang, H. Zhang, X. S. Li, A. Tuladhar, M. Bowden, H.-F. Wang, S. B. Clark and K. M. Rosso, *J. Phys. Chem. C*, 2020, **124**, 5275-5285.

17. T. R. Graham, M. Dembowski, E. Martinez-Baez, X. Zhang, N. R. Jaegers, J. Hu, M. S. Gruszkiewicz, H. W. Wang, A. G. Stack, M. E. Bowden, C. H. Delegard, G. K. Schenter, A. E. Clark, S. B. Clark, A. R. Felmy, K. M. Rosso and C. I. Pearce, *Inorg Chem*, 2018, **57**, 11864-11873.

18. M. Dembowski, M. M. Snyder, C. H. Delegard, J. G. Reynolds, T. R. Graham, H. W. Wang, Leavy, II, S. R. Baum, O. Qafoku, M. S. Fountain, K. M. Rosso, S. B. Clark and C. I. Pearce, *Phys Chem Chem Phys*, 2020, **22**, 4368-4378.

19. S. Wang, X. Zhang, T. R. Graham, H. Zhang, C. I. Pearce, Z. Wang, S. B. Clark, W. Jiang and K. M. Rosso, *CrystEngComm*, 2020, **22**, 2555-2565.

20. N. Phambu, B. Humbert and A. Burneau, *Langmuir*, 2000, **16**, 6200-6207.

21. Y.-H. Chang, H.-Y. Hsu and W.-L. Lin, *Materials Letters*, 2017, **194**, 202-204.

22. F. Zhong, J. Schwabe, R. Thomann and R. Mulhaupt, *Macromol Rapid Commun*, 2019, **40**, e1900015.

23. S. E. Yalcin, B. A. Legg, M. Yesilbas, N. S. Malvankar and J. F. Boily, *Sci Adv*, 2020, **6**, eaaz9708.

24. M. Sassi, E. D. Walter, O. Qafoku, K. M. Rosso and Z. Wang, *J. Phys. Chem. C*, 2020, **124**, 22185-22191.

25. Z. Wang, E. D. Walter, M. Sassi, X. Zhang, H. Zhang, X. S. Li, Y. Chen, W. Cui, A. Tuladhar, Z. Chase, A. D. Winkelman, H. F. Wang, C. I. Pearce, S. B. Clark and K. M. Rosso, *J Hazard Mater*, 2020, **398**, 122853.

26. S. E. Smart, J. Vaughn, I. Pappas and L. Pan, *Chem Commun (Camb)*, 2013, **49**, 11352-11354.

27. K. Wen, J. Wei, H. He, J. Zhu and Y. Xi, *Applied Clay Science*, 2019, **180**.

28. W. H. Casey, M. M. Olmstead and B. L. Phillips, *Inorg Chem*, 2005, **44**, 4888-4890.

29. Z. Chen, Z. Luan, Z. Jia and X. Li, *J. Mater. Sci.*, 2009, **44**, 3098-3111.

30. J. T. Gatlin, Z. L. Mensinger, L. N. Zakharov, D. Macinnes and D. W. Johnson, *Inorg Chem*, 2008, **47**, 1267-1269.

31. W. Seichter, H.-J. Mögel, P. Brand and D. Salah, *Eur. J. Inorg. Chem.*, 1998, **1998**, 795-797.

32. W. Wang, K. M. Wentz, S. E. Hayes, D. W. Johnson and D. A. Keszler, *Inorg Chem*, 2011, **50**, 4683-4685.

33. C. Sweegers, H. Meekes, W. J. P. van Enckevort, I. D. K. Hiralal and A. Rijkeboer, *Cryst Growth Des*, 2004, **4**, 185-198.

34. H. Saalfeld and M. Wedde, *Z Kristallogr*, 1974, **139**, 129-135.

35. A. Vyalikh, K. Zesewitz and U. Scheler, *Magn Reson Chem*, 2010, **48**, 877-881.

36. J. D. Gale, A. L. Rohl, V. Milman and M. C. Warren, *J. Phys. Chem. B*, 2001, **105**, 10236-10242.

37. H. D. Ruan, R. L. Frost and J. T. Kloprogge, *J. Raman Spectrosc.*, 2001, **32**, 745-750.

38. S. B. Clark, M. Buchanan and B. Wilmarth, *Basic research needs for environmental management*, Pacific Northwest National Lab.(PNNL), Richland, WA (United States), 2016.

39. K. Wefers, *Alcoa Technical Paper*, 1987, **19**, 18.

40. X. Li, D. Wang, Q. Zhou, G. Liu and Z. Peng, *Hydrometallurgy*, 2011, **106**, 93-98.

41. H. Zhang, X. Zhang, T. R. Graham, C. I. Pearce, H. Hlushko, J. A. LaVerne, L. Liu, S. Wang, S. Zheng, Y. Zhang, S. B. Clark, P. Li, Z. Wang and K. M. Rosso, *Inorg Chem*, 2021, DOI: 10.1021/acs.inorgchem.1c01111.

42. J. Z. Hu, X. Zhang, N. R. Jaegers, C. Wan, T. R. Graham, M. Hu, C. I. Pearce, A. R. Felmy, S. B. Clark and K. M. Rosso, *J. Phys. Chem. C*, 2017, **121**, 27555-27562.

43. L. Allouche, C. Huguenard and F. Taulelle, *Journal of Physics and Chemistry of Solids*, 2001, **62**, 1525-1531.

44. R. W. Cheary and A. Coelho, *J. Appl. Crystallogr*, 1992, **25**, 109-121.

45. D. Ectors, F. Goetz-Neunhoeffer and J. Neubauer, *J. Appl. Crystallogr*, 2015, **48**, 1998-2001.

46. P. W. Stephens, *J. Appl. Crystallogr*, 1999, **32**, 281-289.

47. A. Hoeher, S. Mergelsberg, O. J. Borkiewicz, P. M. Dove and F. M. Michel, *Acta Cryst. A*, 2019, **75**, 758-765.

48. B. H. Toby and R. B. Von Dreele, *J. Appl. Crystallogr*, 2013, **46**, 544-549.

49. P. Juhás, T. Davis, C. L. Farrow and S. J. L. Billinge, *J. Appl. Crystallogr*, 2013, **46**, 560-566.

50. C. L. Farrow, P. Juhas, J. W. Liu, D. Bryndin, E. S. Bozin, J. Bloch, T. Proffen and S. J. Billinge, *J Phys Condens Matter*, 2007, **19**, 335219.

51. T. Proffen and R. B. Neder, *J. Appl. Crystallogr*, 1999, **32**, 838-839.

52. S. J. Freij, G. M. Parkinson and M. M. Reyhani, *J. Cryst. Growth*, 2004, **260**, 232-242.

53. H. J. You and J. X. Fang, *Nano Today*, 2016, **11**, 145-167.

54. C. V. Chandran, C. E. A. Kirschhock, S. Radhakrishnan, F. Taulelle, J. A. Martens and E. Breynaert, *Chem Soc Rev*, 2019, **48**, 134-156.

55. C. Martineau, F. Taulelle and M. Haouas, *PATAI'S Chemistry of Functional Groups*, 2009, 1-51.

56.   T. W. Swaddle, J. Rosenqvist, P. Yu, E. Bylaska, B. L. Phillips and W. H. Casey, *Science*, 2005, **308**, 1450-1453.
57.   H.-I. Kim and S. K. Lee, *Am. Mineral.*, 2021, **106**, 389-403.
58.   S. R. Egorova, A. N. Mukhamed'yarova and A. A. Lamberov, *Russian Journal of Applied Chemistry*, 2015, **88**, 758-768.
59.   H. Liu, J. S. Tse, J. Hu, Z. Liu, L. Wang, J. Chen, D. J. Weidner, Y. Meng, D. Hausermann and H. K. Mao, *J Phys Chem B*, 2005, **109**, 8857-8860.
60.   S. L. Wang and C. T. Johnston, *Am. Mineral.*, 2000, **85**, 739-744.
61.   M. Wang and M. Muhammed, *Nanostructured Materials*, 1999, **11**, 1219-1229.